

# Predicting S-Duct Flow Using a Composite Algebraic Stress Model

T. Jongen\* and G. Mompean†

Swiss Federal Institute of Technology, 1015 Lausanne, Switzerland  
and

T. B. Gatski‡

NASA Langley Research Center, Hampton, Virginia 23681

**An incompressible composite algebraic stress model is presented that accounts for dissipation rate anisotropies and that is validated against S-duct flow. The component algebraic stress and algebraic, anisotropic dissipation rate models have been developed previously, and tested against homogeneous flow. The composite model is developed for integration to the wall and is calibrated against high-Reynolds number plane channel flow data to ensure the correct log-law behavior. The model is validated and analyzed against turbulent flow in an S duct. Both predicted mean flow quantities and turbulence statistics are compared with experimental data, as well as with an isotropic eddy viscosity model and an algebraic stress model with an isotropic dissipation rate. The experimentally observed lag between the shear stress vector direction and the mean velocity-gradient vector direction is qualitatively predicted. The effects of anisotropic dissipation rate on the production of the dissipation term in the dissipation rate equation and on the scalar functions that multiply the linear and nonlinear terms in the tensor expansion are examined relative to the algebraic stress formulation with an isotropic eddy viscosity.**

## I. Introduction

WITH the constantly increasing demands on the predictive capability of the Reynolds averaged Navier–Stokes (RANS) formulation for complex, aerodynamic turbulent flowfields, the need for more accurate and more complete turbulent closures has also escalated. This results in an inherent demand for the incorporation of more physics into the models, which then allows for better predictive performance. Although the incorporation of physics is relatively straightforward in phenomenological approaches, this step is more challenging when some mathematical rigor is enforced. Because complicated physical processes occur in engineering flows, the particular extra effects that should be incorporated into the models are not always obvious. Nevertheless, even in the existing higher-order closures, such as second-moment or Reynolds stress closures, several assumptions have been made. Unknown correlations such as the pressure–velocity transport term and the tensor turbulent dissipation rate require closure. In the former case, incompressibility modelers have either explicitly neglected the term with the argument that it is small or have included the term in the model for the total turbulent transport. (Lumley<sup>1</sup> argued that this term could be at least 20% of the triple-velocity correlation, which would preclude neglecting the term a priori.) For the turbulent dissipation rate, most modelers have implicitly included the dissipation rate anisotropies into the pressure–strain correlation. Any explicit accounting of these anisotropies through models for the deviatoric part of the tensor dissipation rate have previously assumed a direct correlation with the turbulent Reynolds stresses.<sup>2</sup> Recently, some interest has been evident in the development of alternatives that do not directly couple the behavior of the dissipation rate anisotropies to that of the Reynolds stresses. These alternatives<sup>3,4</sup> include the development of evolution equations for the tensor dissipation rate directly; these equations by

their structure incorporate redistribution and transport effects into the determination of the tensor dissipation rate components. The focus of this study is the adaptation of an anisotropic dissipation rate model for practical implementation and application to engineering flows.

Although such a model can be readily calibrated in homogeneous turbulent flows by solving its (ordinary) differential form, application to inhomogeneous flows requires the solution of an additional set of six partial differential transport equations. When coupled with a full second-moment transport model for the turbulent stresses, this requires the solution of 12 transport equations for the turbulent correlations alone, which is clearly outside the range of any engineering application.

Recently, explicit algebraic stress models have received renewed attention.<sup>5,6</sup> These nonlinear extensions to a two-equation formulation such as  $K-\varepsilon$  allow for the inclusion of stress anisotropies in the formulation, while the computational cost remains at the level of a two-equation formulation. In addition, these models have been tested on a variety of incompressible (and compressible) engineering flows using both the  $K-\varepsilon$  formulation<sup>7,8</sup> and the  $K-\omega$  formulation.<sup>9</sup> The results from these studies indicate that the explicit algebraic approach is a viable approximation to the full Reynolds stress closure for a variety of engineering flows. This paper extends a coupled algebraic stress and anisotropic dissipation rate formulation<sup>10</sup> to inhomogeneous flows by evaluating this composite model against the performance characteristics of an explicit algebraic stress model (EASM) with an isotropic dissipation rate.

In the next section, the relevant differential formulations for the Reynolds stress and anisotropic dissipation rate are presented for completeness. The resulting explicit algebraic stress and dissipation rate models are also summarized. The models are then coupled with the  $K-\varepsilon$  two-equation formulation, and a composite model suitable for integration to the wall is derived.

In Sec. III, the composite model is calibrated against channel flow to ensure that the correct log-layer features are retained. In simple, inhomogeneous flows such as channels, dissipation rate anisotropies are confined mainly to near-wall regions. Thus, to assess the predictive capability of the composite model, it is necessary to examine a complex flow where these added anisotropic effects may be necessary to successfully compute the flow outside the near-wall region. One such flow, which has received significant attention, is the S-duct flow.<sup>11</sup> The transverse pressure gradient generated by the curved side walls creates streamwise vorticity, which introduces

Received May 29, 1997; revision received Oct. 31, 1997; accepted for publication Nov. 10, 1997. Copyright © 1997 by the American Institute of Aeronautics and Astronautics, Inc. No copyright is asserted in the United States under Title 17, U.S. Code. The U.S. Government has a royalty-free license to exercise all rights under the copyright claimed herein for Governmental purposes. All other rights are reserved by the copyright owner.

\*Research Assistant, Fluid Mechanics Laboratory, Department of Mechanical Engineering.

†Senior Researcher, Fluid Mechanics Laboratory, Department of Mechanical Engineering.

‡Senior Research Scientist, Aerodynamic and Acoustic Methods Branch.

three-dimensional effects into the flow. For validation studies, duct flows have an advantage over open flow configurations in that the Reynolds number and the strength of the three-dimensional effects can be more easily varied and a better spatial resolution can be achieved due to the relatively thick boundary layers. This particular flow experiment is also ideally suited for computational validation because it consists of a quasi-two-dimensional inlet flow, followed by a curved wall section, and then a relaxation region where the flow recovers back to a two-dimensional form. Comparisons with experimental results<sup>11</sup> are made to validate the model predictions and to evaluate the influence of anisotropic stress and dissipation effects on the flowfields.

## II. Nonlinear Two-Equation Formulation

Unlike the usual isotropic eddy viscosity models that couple a Boussinesq approximation for the turbulent stresses with the mean momentum equations, the nonlinear two-equation approach involves a more complex relationship between the turbulent stresses and the mean flowfield. This increased complexity appears as an explicit functional dependency of the eddy viscosity on the mean velocity gradients, as well as a nonlinear extension to the linear dependency on the mean strain rate field that appears in the Boussinesq eddy viscosity constitutive relationship.

In this section, both anisotropic stress and dissipation rate effects are included in the formulation through explicit algebraic relationships for the stress and dissipation rate tensors. An outline of how these extra effects appear in the formulation of the mean flow and turbulent transport equations is presented.

### A. Mean Flow and Turbulent Transport Equations

The mean quantities of an incompressible turbulent flow are obtained from a solution of the RANS equations given in nondimensional form as

$$\frac{\partial \bar{u}_j}{\partial x_j} = 0 \quad (1)$$

and

$$\frac{\partial \bar{u}_i}{\partial t} + \bar{u}_j \frac{\partial \bar{u}_i}{\partial x_j} = -\frac{\partial \bar{p}}{\partial x_i} + \frac{1}{Re} \frac{\partial \bar{\sigma}_{ij}}{\partial x_j} - \frac{\partial \tau_{ij}}{\partial x_j} \quad (2)$$

where  $\bar{u}_i$  and  $\bar{p}$  are the mean velocity and pressure, respectively, and  $Re$  is the Reynolds number. The right-hand side of the equation also contains both the viscous stress tensor  $\bar{\sigma}_{ij}$ , which is proportional to the mean strain rate, and the turbulent second-moment correlation tensor  $\tau_{ij} \equiv \overline{u'_i u'_j}$ , which requires closure.

In the incompressible formulation for the mean motion, only the turbulent second-moment Reynolds stress tensor needs to be modeled. For the higher-order closures, the transport equation for the  $\tau_{ij}$  correlation is used:

$$\frac{\partial \tau_{ij}}{\partial t} + \frac{\partial}{\partial x_k} (\bar{u}_k \tau_{ij}) = P_{ij} + \Pi_{ij}^d - \varepsilon_{ij} + \frac{\partial D_{ijk}'}{\partial x_k} + \nu \frac{\partial^2 \tau_{ij}}{\partial x_k \partial x_k} \quad (3)$$

where the right-hand side represents the rate of change of  $\tau_{ij}$  produced by the turbulent production  $P_{ij}$ , the deviatoric part of the pressure strain-rate correlation  $\Pi_{ij}^d$ , the turbulent dissipation rate  $\varepsilon_{ij}$ , and the turbulent diffusion  $D_{ijk}'$ .

The deviatoric part of the dissipation rate is generally absorbed into the pressure-strain correlation to account for any anisotropic dissipation rate effects. However, as will be discussed shortly, when models for the anisotropic dissipation rate  $\varepsilon_{ij}$  are utilized, this assimilation into the pressure-strain correlation is no longer necessary.

The trace of Eq. (3) results in the turbulent kinetic energy equation given by

$$\frac{DK}{Dt} = \mathcal{P} - \varepsilon + \frac{\partial \mathcal{D}'_j}{\partial x_j} + \nu \frac{\partial^2 K}{\partial x_j \partial x_j} \quad (4)$$

where  $D/Dt = \partial/\partial t + \bar{u}_j \partial/\partial x_j$  and the right-hand side represents the transport of  $K$  by the turbulent production  $\mathcal{P} \equiv P_{ii}/2$ , the isotropic turbulent dissipation rate  $\varepsilon \equiv \varepsilon_{ii}/2$ , the turbulent diffusion

$\mathcal{D}'_j \equiv D'_{ij}/2$ , and the viscous diffusion. These terms are defined by

$$\mathcal{P} = -\tau_{ij} \frac{\partial \bar{u}_i}{\partial x_j} \quad (4a)$$

$$\varepsilon = \nu \frac{\partial u'_i}{\partial x_j} \frac{\partial u'_i}{\partial x_j} \quad (4b)$$

and

$$\mathcal{D}'_j = -\left[ \frac{1}{2} \overline{u'_i u'_i u'_j} + \frac{\overline{p' u'_i}}{\rho} \delta_{ij} \right] \quad (4c)$$

Consistent with the simplification that results from the two-equation formulation, a simple form for the turbulent transport  $\mathcal{D}'_j$  is usually used:

$$\mathcal{D}'_j = \frac{\nu_t}{\sigma_K} \frac{\partial K}{\partial x_j} \quad (5)$$

with

$$\nu_t = C_\mu (K^2/\varepsilon) \quad (5a)$$

and  $\sigma_K = 1$  and  $C_\mu$  is usually in the range of 0.08–0.09. With this model for the turbulent diffusivity, both the turbulent and molecular diffusion terms can be combined into a gradient transport model with an effective viscosity of  $\nu + \nu_t/\sigma_K$ .

When an anisotropic turbulent dissipation rate formulation is used, the isotropic dissipation rate equation can retain dissipation anisotropies; thus, the form of the  $\varepsilon$  equation is modified. From the recent model of Speziale and Gatski,<sup>3</sup> for the anisotropic dissipation rate, the isotropic ( $\varepsilon = \varepsilon_{ii}/2$ ) dissipation-rate equation can be written as

$$\frac{D\varepsilon}{Dt} = \mathcal{P}_\varepsilon - \mathcal{D}_\varepsilon - 2(1 + \beta)\varepsilon d_{ij} S_{ij} + \frac{\partial}{\partial x_j} \mathcal{D}'_{\varepsilon j} + \nu \frac{\partial^2 \varepsilon}{\partial x_j \partial x_j} \quad (6)$$

where

$$\mathcal{P}_\varepsilon = -C_{\varepsilon 1} \frac{\varepsilon}{K} \tau_{ij} \frac{\partial \bar{u}_i}{\partial x_j} \quad (7a)$$

$$\mathcal{D}_\varepsilon = f_\varepsilon C_{\varepsilon 2} (\varepsilon^2/K) \quad (7b)$$

and  $S_{ij} = (\partial \bar{u}_i/\partial x_j + \partial \bar{u}_j/\partial x_i)/2$  is the strain rate tensor. The first and second terms on the right-hand side are the production and destruction of dissipation, respectively, and the last term is the viscous diffusion. The third term represents an additional production of dissipation by the dissipation rate anisotropy:

$$d_{ij} = \frac{(\varepsilon_{ij} - \frac{2}{3}\varepsilon\delta_{ij})}{2\varepsilon} \quad (8)$$

The dissipation-rate diffusion term is modeled for the two-equation formulation as

$$\mathcal{D}'_{\varepsilon j} = \frac{\nu_t}{\sigma_\varepsilon} \frac{\partial \varepsilon}{\partial x_j} \quad (9)$$

Note that in the destruction of dissipation term (7b) a damping function  $f_\varepsilon$  has been introduced so that the equation set can be integrated directly to the wall. This function removes the singularity in the term at the wall and moves the location of the predicted buffer layer region. Various forms of this function exist, and the function has been calibrated for the isotropic eddy viscosity formulation. It will also need to be calibrated in this study because both stress and dissipation-rate anisotropies are introduced and have an effect on the prediction of the near-wall and log-layer behavior.

The closure constants  $\beta$ ,  $C_{\varepsilon 1}$ ,  $C_{\varepsilon 2}$ , and  $\sigma_\varepsilon$ , as well as the damping function  $f_\varepsilon$ , must now be determined. However, first the turbulent stress  $\tau_{ij}$  and dissipation-rate fields  $\varepsilon_{ij}$  must be specified.

### B. Explicit Algebraic Stress and Dissipation-Rate Models

The derivation and application of the EASM used in this study has been presented previously.<sup>5,7–9</sup> The basis of the explicit model has not changed since the model's inception<sup>5</sup>; however, in the application studies, issues of numerical robustness have surfaced that have required modification to the turbulent eddy viscosity functional dependency to account for regions in which the turbulence is characterized by its rapid distortion limit. A computationally robust formulation for incompressible flows has been proposed<sup>8</sup> and

is the starting point for the derivation outlined here. Note that this extension to account for rapid distortion effects is not unique and that other alternatives have been proposed that strictly adhere to the correct limiting behavior in the rapid distortion limit<sup>12</sup>; however, these alternatives have not been tested in practical engineering applications. Note that regardless of the approach that is used, in the dynamically significant regions of the flows that have been studied thus far these functional extensions do not alter the nonlinear eddy viscosity behavior.

The starting points for the derivation of the algebraic models for both the turbulent stress and dissipation rate anisotropies are 1) the equilibrium assumptions that are imposed on both the convective and diffusive terms that appear in the Reynolds stress transport equations<sup>5</sup> and 2) the anisotropic dissipation rate equations.<sup>3</sup> These constraints are imposed on the anisotropy tensor

$$b_{ij} = \frac{(\tau_{ij} - \frac{2}{3}K\delta_{ij})}{2K} \quad (10)$$

for the Reynolds stress and  $d_{ij}$  [Eq. (8)] for the dissipation rate. This step yields the following set of implicit linear algebraic equations for the anisotropy tensors<sup>3,5,10</sup>:

$$b_{ij}^* + (b_{ik}^* S_{jk}^* + b_{jk}^* S_{ik}^* - \frac{2}{3} b_{mn}^* S_{mn}^* \delta_{ij}) - (b_{ik}^* W_{kj}^* - W_{ik}^* b_{kj}^*) = -S_{ij}^* - g d_{ij}^* \quad (11)$$

$$d_{ij}^* - (\beta_2/\alpha_3)(d_{ik}^* S_{jk}^* + d_{jk}^* S_{ik}^* - \frac{2}{3} d_{mn}^* S_{mn}^* \delta_{ij}) - (\beta_1/\alpha_2)(d_{ik}^* W_{kj}^* - W_{ik}^* d_{kj}^*) = -(2g_\varepsilon/15\alpha_1)S_{ij}^* \quad (12)$$

where

$$b_{ij}^* = (\alpha_3/\alpha_1)b_{ij}, \quad d_{ij}^* = (\alpha_3/\alpha_1)d_{ij} \quad (13a)$$

$$S_{ij}^* = \alpha_3 \frac{K}{\varepsilon} S_{ij}, \quad S_{ij} = \frac{1}{2} \left( \frac{\partial \bar{u}_i}{\partial x_j} + \frac{\partial \bar{u}_j}{\partial x_i} \right) \quad (13b)$$

$$W_{ij}^* = \alpha_2 \frac{K}{\varepsilon} W_{ij}, \quad W_{ij} = \frac{1}{2} \left( \frac{\partial \bar{u}_i}{\partial x_j} - \frac{\partial \bar{u}_j}{\partial x_i} \right) \quad (13c)$$

$$\alpha_1 = \left( \frac{4}{3} - C_2 \right) (g/2), \quad \alpha_2 = (2 - C_4) (g/2) \quad (13d)$$

$$\alpha_3 = (2 - C_3) (g/2)$$

$$\beta_1 = \left( \frac{7}{11} \beta_3 + \frac{1}{11} \right) g_\varepsilon, \quad \beta_2 = \left( \frac{15}{11} \beta_3 - \frac{1}{11} \right) g_\varepsilon \quad (13e)$$

$$g = \frac{1}{(C_1/2) + C_g - 1}, \quad g_\varepsilon = \frac{1}{C_{\varepsilon 5} + C_{g_\varepsilon} - 1} \quad (13f)$$

with  $C_1 = 6.8$ ,  $C_2 = 0.36$ ,  $C_3 = 1.25$ , and  $C_4 = 0.40$ . This set of coefficients is based on the Speziale, Sarkar, and Gatski (SSG) pressure-strain correlation model<sup>13</sup> and has been used in a variety of test flow calculations.<sup>7-9</sup> In the SSG model, the coefficient  $C_1$  is dependent on the production-to-dissipation ratio ( $C_1 = 3.4 + 1.8\mathcal{P}/\varepsilon$ ), and the value of  $C_1 = 6.8$  is based on the calibrated equilibrium value for this ratio in homogeneous shear flow ( $\mathcal{P}/\varepsilon = 1.88$ ). In the composite model, a slightly different calibrated equilibrium value for the  $\mathcal{P}/\varepsilon$  ratio is obtained, and this value is used to determine  $C_1$ , as well as the coefficients  $C_g$  and  $C_{g_\varepsilon}$ , which are the values of  $\mathcal{P}/\varepsilon$  for homogeneous shear flow. These constant coefficients will be fixed in the next section. From the development and calibration of the anisotropic dissipation rate model,<sup>3</sup>

$$C_{\varepsilon 5} = 5.8, \quad \beta_3 = 0.6 \quad (14)$$

Equations (11) and (12) are the starting points for the algebraic stress and dissipation rate formulations.

Equations (11) and (12) both fit into the general functional form

$$F_{ij}^* + a_1 \left( F_{ik}^* S_{jk}^* + F_{jk}^* S_{ik}^* - \frac{2}{3} F_{mn}^* S_{mn}^* \delta_{ij} \right) + a_2 (F_{ik}^* W_{kj}^* - W_{ik}^* F_{kj}^*) = - \sum_{\lambda} L^{(\lambda)} T_{ij}^{(\lambda)} \quad (15)$$

where  $a_1$  and  $a_2$  are constants,  $F_{ij}^*$  represents either  $b_{ij}^*$  or  $d_{ij}^*$ , and

$$T_{ij}^{(1)} = S_{ij}^*, \quad T_{ij}^{(2)} = (S_{ik}^* W_{kj}^* + S_{jk}^* W_{ki}^*) \quad (16)$$

$$T_{ij}^{(3)} = (S_{ik}^* S_{kj}^* - \frac{1}{3} S_{mn}^* S_{mn}^* \delta_{ij})$$

form the three-term integrity basis ( $\lambda = 1, 2, 3$ ) for functions of a symmetric and an antisymmetric tensor. The  $L^{(\lambda)}$  are either constants or, more generally, scalar functions of the irreducible invariants of  $S_{ij}^*$  and  $W_{ij}^*$ . Note that this three-term expansion is only formally valid for two-dimensional flows. For three-dimensional flows, the 10-term basis would be required; however, Gatski and Speziale<sup>5</sup> have shown that the three-term basis is a truncation of the full tensorial expansion of the lowest order. For this reason and because the full 10-term basis is too cumbersome for practical calculations, the three-term basis is recommended for both two- and three-dimensional flows. The solution to this system is the polynomial expansion

$$F_{ij}^* = \sum_{\lambda} G^{(\lambda)} T_{ij}^{(\lambda)} \quad (17)$$

where  $G^{(\lambda)}$  are also scalar functions of the irreducible invariants of  $S_{ij}^*$  and  $W_{ij}^*$  given by

$$G^{(1)} = -C^* (L^{(1)} + 2a_2 \zeta^2 L^{(2)} - (a_1/3) \eta^2 L^{(3)}) \quad (18)$$

$$G^{(2)} = -a_2 G^{(1)} - L^{(2)} = C^* [a_2 L^{(1)} - (1 - \frac{2}{3} a_1^2 \eta^2) L^{(2)} - (a_1 a_2/3) \eta^2 L^{(3)}] \quad (19)$$

$$G^{(3)} = -2a_1 G^{(1)} - L^{(3)} = C^* [2a_1 L^{(1)} + 4a_1 a_2 \zeta^2 L^{(2)} - (1 + 2a_1^2 \zeta^2) L^{(3)}] \quad (20)$$

with

$$C^* = \frac{1}{(1 - \frac{2}{3} a_1^2 \eta^2 + 2a_2^2 \zeta^2)} \quad (21)$$

$$\eta = \alpha_3 (K/\varepsilon) (S_{ij} S_{ij})^{\frac{1}{2}}, \quad \zeta = \alpha_2 (K/\varepsilon) (W_{ij} W_{ij})^{\frac{1}{2}} \quad (22)$$

Unfortunately, singularities may appear in the coefficients for some values of the scalar invariants. This problem has been treated previously by a regularization procedure that retains the correct functional behavior away from the singularity but yields finite values in the vicinity of the singularity.<sup>5</sup> In addition, as more practical flow problems have been solved, alternate regularizations have been used to increase the robustness and applicability of the models.<sup>7-10</sup> Fortunately, throughout this study, it has been found that the non-regularized form of  $C^*$  given in Eq. (21) was sufficient. Thus, it was not necessary to complicate the performance analysis with the introduction of the regularized forms for  $C^*$ .

The EASM that is obtained from Eq. (11) with  $d_{ij}^* = 0$  leads to  $a_1 = 1$ ,  $a_2 = -1$ ,  $L^{(1)} = 1$ , and  $L^{(2)} = L^{(3)} = 0$  in Eq. (15) and

$$b_{ij}^* = -C_{\mu}^* [S_{ij}^* + (S_{ik}^* W_{kj}^* + S_{jk}^* W_{ki}^*) - 2(S_{ik}^* S_{kj}^* - \frac{1}{3} S_{kl}^* S_{kl}^* \delta_{ij})] \quad (23)$$

where

$$C_{\mu}^* = \frac{1}{(1 - \frac{2}{3} \eta^2 + 2\zeta^2)} \quad (24)$$

One goal of this study is to evaluate the performance of a composite algebraic stress and dissipation rate model. Toward this end, the coupled set of linear algebraic equations (11) and (12) must be solved. The explicit algebraic polynomial expansion<sup>3</sup> for  $d_{ij}^*$  from Eq. (12) can also be obtained directly from a comparison with Eq. (15). This comparison yields  $a_1 = -(\beta_2/\alpha_3)$ ,  $a_2 = -(\beta_1/\alpha_2)$ ,  $L^{(1)} = (2g_\varepsilon/15\alpha_1)$ , and  $L^{(2)} = L^{(3)} = 0$ , which gives the explicit relationship<sup>3</sup>

$$d_{ij}^* = -(2g_\varepsilon/15\alpha_1) C_{\mu\varepsilon}^* [S_{ij}^* + (\beta_1/\alpha_2) (S_{ik}^* W_{kj}^* + S_{jk}^* W_{ki}^*) + 2(\beta_2/\alpha_3) (S_{ik}^* S_{kj}^* - \frac{1}{3} S_{mn}^* S_{mn}^* \delta_{ij})] \quad (25)$$

where

$$C_{\mu\epsilon}^* = \frac{1}{\left[1 - \frac{2}{3}(\beta_2/\alpha_3)^2\eta^2 + 2(\beta_1/\alpha_2)^2\zeta^2\right]} \quad (26)$$

Because the dissipation rate anisotropy  $d_{ij}^*$  is independent of the stress anisotropy  $b_{ij}^*$ , the explicit representation for  $d_{ij}^*$  given in Eq. (25) can be directly substituted into Eq. (11) to yield an implicit relation for the algebraic stress model<sup>10</sup> given by

$$\begin{aligned} & b_{ij}^* + (b_{ik}^* S_{jk}^* + b_{jk}^* S_{ik}^* - \frac{2}{3} b_{mn}^* S_{mn}^* \delta_{ij}) - (b_{ik}^* W_{kj}^* - W_{ik}^* b_{kj}^*) \\ &= -(1 + \mathcal{A}_1) S_{ij}^* - \mathcal{A}_2 (S_{ik}^* W_{kj}^* + S_{jk}^* W_{ki}^*) \\ & - 2\mathcal{A}_3 (S_{ik}^* S_{kj}^* - \frac{1}{3} S_{mn}^* S_{mn}^* \delta_{ij}) \end{aligned} \quad (27)$$

where

$$\mathcal{A}_1 = \frac{-2g\epsilon}{15\alpha_1} C_{\mu\epsilon}^*, \quad \mathcal{A}_2 = \frac{\beta_1}{\alpha_2} \mathcal{A}_1, \quad \mathcal{A}_3 = \frac{\beta_2}{\alpha_3} \mathcal{A}_1 \quad (28)$$

Note that Eq. (27) has the same functional form as Eq. (15) even when  $d_{ij}^* \neq 0$ . Also recognize that anisotropic dissipation rate effects have now been incorporated into the formulation through the coefficients  $\mathcal{A}_i$ . If these coefficients are zero ( $C_{\mu\epsilon}^* = 0$ ), then Eq. (27) reduces to the implicit linear algebraic expression given in Eq. (11) with  $d_{ij}^* = 0$ . A comparison of the form of Eq. (27) with that of Eq. (15) yields the coefficients  $a_1 = 1$ ,  $a_2 = -1$ ,  $L^{(1)} = 1 + \mathcal{A}_1$ , and  $L^{(2)} = \mathcal{A}_2$ ,  $L^{(3)} = 2\mathcal{A}_3$ . The  $G^{(\lambda)}$  are, then,

$$\begin{aligned} G^{(1)} &= -C_{\mu}^* \left\{ 1 + \mathcal{A}_1 \left[ 1 - 2(\beta_1/\alpha_2)\zeta^2 - \frac{2}{3}(\beta_2/\alpha_3)\eta^2 \right] \right\} \\ G^{(2)} &= -C_{\mu}^* \left\{ 1 + \mathcal{A}_1 \left[ 1 + (\beta_1/\alpha_2) \left( 1 - \frac{2}{3}\eta^2 \right) - \frac{2}{3}(\beta_2/\alpha_3)\eta^2 \right] \right\} \\ G^{(3)} &= +2C_{\mu}^* \left\{ 1 + \mathcal{A}_1 \left[ 1 - (\beta_2/\alpha_3)(1 + 2\zeta^2) - 2(\beta_1/\alpha_2)\zeta^2 \right] \right\} \end{aligned} \quad (29)$$

The final explicit polynomial expression for  $\tau_{ij}$ , which includes the effects of anisotropic dissipation rate, is then given by<sup>10</sup>

$$\begin{aligned} \tau_{ij} &= \frac{2}{3} K \delta_{ij} + 2K (\alpha_1/\alpha_3) \left[ G^{(1)} S_{ij}^* + G^{(2)} (S_{ik}^* W_{kj}^* + S_{jk}^* W_{ki}^*) \right. \\ & \left. + G^{(3)} (S_{ik}^* S_{kj}^* - \frac{1}{3} S_{kl}^* S_{kl}^* \delta_{ij}) \right] \end{aligned} \quad (30)$$

This explicit algebraic relationship is now coupled with Eq. (4) for the turbulent kinetic energy and Eq. (6) for the turbulent dissipation rate. A further simplification to Eq. (6), which assimilates the dissipation anisotropy term into the production of dissipation term, has been proposed by Speziale and Gatski.<sup>3</sup> By using Eq. (25) and the assumption of equilibrium, the dissipation rate equation [Eq. (6)] reduces to the form

$$\frac{D\epsilon}{Dt} = C_{\epsilon 1}^* \frac{\epsilon}{K} \mathcal{P} - f_{\epsilon} C_{\epsilon 2}^* \frac{\epsilon^2}{K} + \frac{\partial}{\partial x_k} \left[ \left( \nu + \frac{\nu_t}{\sigma_{\epsilon}} \right) \frac{\partial \epsilon}{\partial x_k} \right] \quad (31)$$

where

$$C_{\epsilon 1}^* = C_{\epsilon 1} + \frac{2g_{\epsilon}(1 + \beta)}{15C_{\mu}} C_{\mu\epsilon}^* \quad (32)$$

with

$$C_{\epsilon 2} = 1.83, \quad \beta = \frac{3}{4} \left( \frac{14}{11} \beta_3 - \frac{16}{33} \right) \quad (33a)$$

$$\sigma_{\epsilon} = \frac{\kappa^2}{(C_{\epsilon 2} - C_{\epsilon 1}^*)} \frac{C_{\mu}}{\sqrt{C_{\mu}^*{}^3}}, \quad \kappa = 0.41 \quad (33b)$$

$$f_{\epsilon} = [1 - \exp(-y^+/5.2)]^2, \quad y^+ = y u_{\tau} / \nu \quad (33c)$$

where the subscript  $l$  denotes the log-layer value,  $u_{\tau}$  is the shear velocity, and  $y$  is taken as the distance normal to the surface.

### III. Calibration and Validation

To finalize the composite model, the closure coefficients that have not been specified must be calibrated. From the discussion of the algebraic stress and dissipation rate equations (11) and (12), the coefficients  $C_1$ ,  $C_g$ , and  $C_{g\epsilon}$ , which are related to  $\mathcal{P}/\epsilon$ , must be evaluated; from Eq. (32),  $C_{\epsilon 1}$  must be determined as well. These coefficients are determined from a calibration with the equilibrium results from a direct numerical simulation (DNS) of homogeneous shear flow<sup>14</sup> and are given by

$$C_g = C_{g\epsilon} = 1.85, \quad C_1 = 6.73, \quad C_{\epsilon 1} = 1.20 \quad (34)$$

As shown in Table 1, the calibration of the composite model provides a good approximation to the DNS results for the anisotropy tensor  $b_{ij}$ , the nondimensional shear rate  $SK/\epsilon$ , and the  $\mathcal{P}/\epsilon$  ratio. The results from the composite model are also in close agreement with the results from the algebraic dissipation rate model (ADRM) coupled with a full Reynolds stress model<sup>3</sup> (RSM).

The formulation presented for both the EASM model and the composite model does not include any of the regularization modifications that have been proposed previously.<sup>8,12</sup> These regularizations account for flows with strong shear rates that cause singularities in the  $C_{\mu}^*$  coefficient. Figure 1 shows the behavior of the two models in the  $(III_b, -II_b)$  phase space (where  $III_b = b_{ip}b_{pq}b_{qi}/3$  and  $II_b = -b_{ip}b_{pi}/2$ ) for a wide range of nondimensional shear rates. As expected from the comparison with the DNS results (Table 1), both models closely approximate the invariant values from the DNS as well. However, the composite model is better able to capture the effect of high shear rates by tracking toward the one-component limit of the invariant map. The nonregularized EASM model saturates in the middle of the phase plane.

In Eq. (33b), the coefficients  $C_{\epsilon 1}^* \approx 1.45$  and  $C_{\mu}^* \approx 0.079$  are the values of  $C_{\epsilon 1}^*$  and  $C_{\mu}^*$  found in the log layer of channel flow with  $C_{\mu} = 0.094$ ; in Eq. (33c), the function  $f_{\epsilon}$  is calibrated against the channel flow data. Figure 2 shows the model predictions for the log law, the turbulent kinetic energy, and the turbulent stress components compared with both the experimental data of Laufer<sup>15</sup> at a Reynolds number (based on bulk velocity and channel width) of 61,600 and

Table 1 Equilibrium values for homogeneous shear flow

Equilibrium values	Composite model	ADRM with RSM	DNS
$b_{11}$	0.200	0.200	0.215
$b_{12}$	-0.155	-0.153	-0.158
$b_{22}$	-0.139	-0.139	-0.153
$b_{33}$	-0.061	-0.061	-0.062
$SK/\epsilon$	5.98	5.95	5.70
$\mathcal{P}/\epsilon$	1.85	1.83	1.85

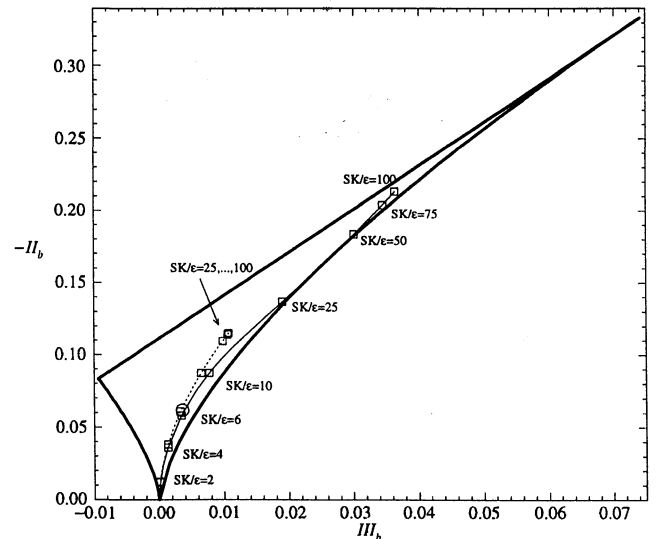


Fig. 1 Homogeneous shear phase plane mapping of EASM and composite model for different shear rates ( $SK/\epsilon$ ,  $\square$ );  $\circ$ , DNS ( $SK/\epsilon = 5.70$ ); —, composite model; and ---, EASM.

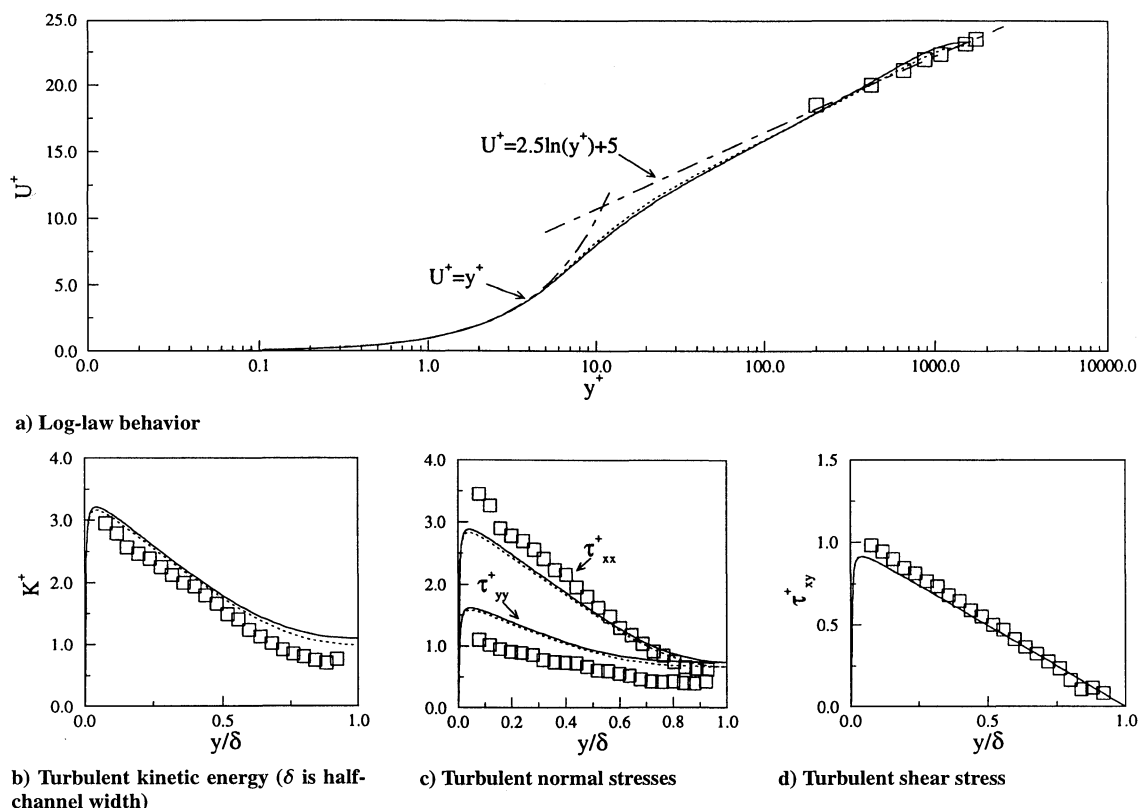


Fig. 2 Composite model calibration for incompressible channel flow:  $\square$ , experiment; —, composite model; and ---, EASM.

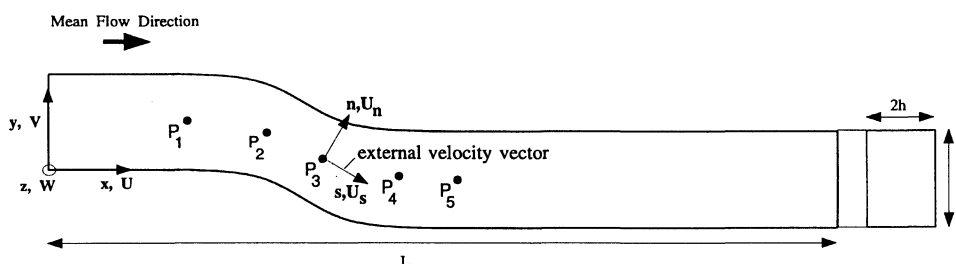


Fig. 3 Top view of three-dimensional S-duct geometry.

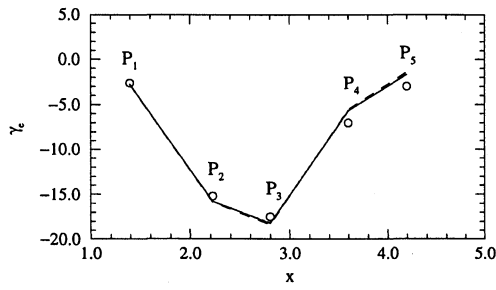
the EASM results. As shown in Fig. 2 the new composite model, as well as the previously developed EASM, replicates the log law quite well and also yields good overall agreement with the turbulence quantities.

The composite model is tested here against a complex internal flow case, and the results are compared with the experimental results. The S-duct test case is ideally suited for computational validation because it consists of a quasi-two-dimensional inlet flow, followed by the curved wall section and then a relaxation region where the flow recovers back to a two-dimensional form. Unlike straight duct flows where differences in the turbulent normal stresses induce streamwise vorticity, the curved section of the S-duct flow, through the transverse pressure gradient, generates a streamwise vorticity, which enhances the turbulent stress anisotropy in the flowfield.

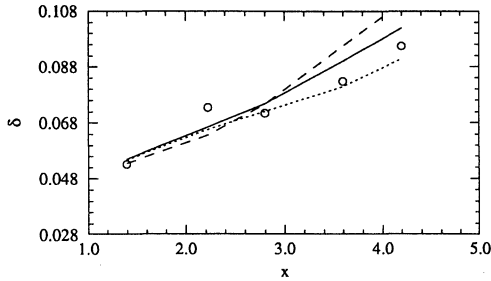
A top view of the S-duct geometry is shown in Fig. 3 along with the relative positions of the measuring stations along the duct. The entire length of the duct  $L$  is 8.1 m; the upstream section is 1.1 m long, the S section is 3 m long, and the downstream section is 4 m long. The inlet Reynolds number is  $10^6$  based on the centerline velocity and half-height  $h$ . This S-duct experiment<sup>11</sup> is an extension of previous work<sup>16</sup> and is characterized by a stronger bend. The results presented here are the first full Navier–Stokes computations performed on this geometry. In the S duct, it is the development of the boundary layer on the flat bottom surface ( $z = 0$ ) that is studied. The boundary layer is made three dimensional and the enhanced stress anisotropy is promoted by way of the transverse ( $y$  direction in Fig. 3) pressure gradient generated by the curved side walls. In

this test, three models are compared: an isotropic eddy viscosity model (EVM),<sup>17</sup> the EASM,<sup>5</sup> and the new composite model.

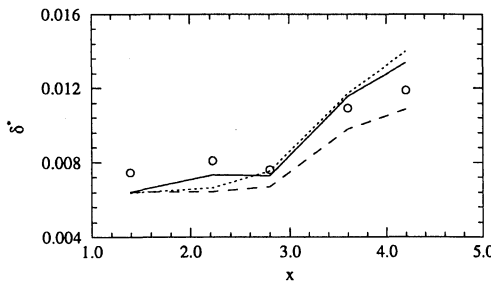
The computations are performed by using a finite volume method<sup>18</sup> with a cell-centered discretization. Grid dependence tests have been performed with three grids having a different number of cells in the  $y$  and  $z$  directions: a coarse grid consisting of  $46 \times 25 \times 25$  elements in the  $x$ ,  $y$ , and  $z$  directions, respectively; a finer grid having  $46 \times 50 \times 50$  elements; and the finest grid having  $46 \times 50 \times 100$  elements. The differences between the results obtained on the two finer grids were very small, suggesting that further mesh refinement was not necessary. For this reason, the quantities presented here are deduced from the calculations done with the intermediate grid ( $46 \times 50 \times 50$  elements). The inlet conditions, taken from experiment,<sup>11</sup> have shown that the boundary layer developing along the bottom wall ( $z = 0$ ) is two dimensional over most of the inlet plane ( $x = 0$ ). Because the interest of the S-duct experiment is to study the effect of transverse pressure gradients on an initially two-dimensional boundary layer, it is important to have good resolution on the bottom wall. This was attained because the first cell center was located on average at  $z^+ \approx 0.25$  along the bottom wall. Of lesser importance were the effects of the side walls, which were used to attain a transverse pressure gradient that forces the flow to follow the two consecutive bends. Wall functions, therefore, have been used for the two side walls because it is less crucial to capture here the boundary layers developing on these curved side walls than the subsequent transverse pressure gradient. Because the flow is symmetric in the  $z$  direction, only half the duct was computed. This



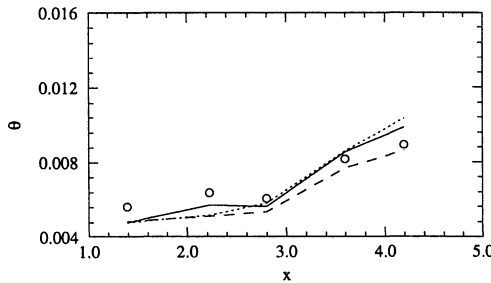
a) Freestream velocity angle  $\gamma_e$



b) Boundary-layer thickness  $\delta$



c) Displacement thickness  $\delta^*$

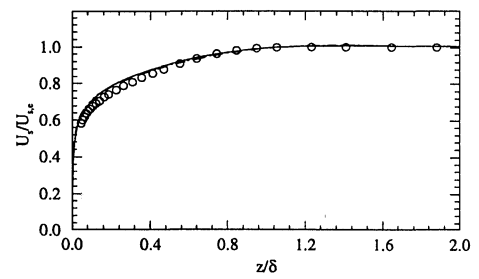


d) Momentum thickness  $\theta$

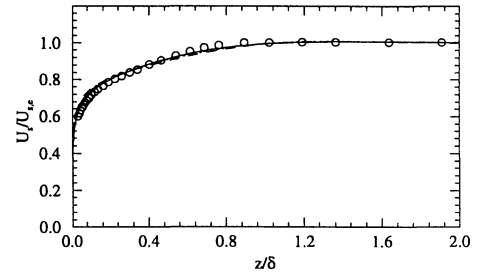
**Fig. 4 Streamwise variation of mean flow properties along duct centerline:  $\circ$ , experiment; —, composite model; ---, EASM; and - - -, EVM.**

also minimizes grid points and allows for a greater concentration of points in the  $z$  direction.

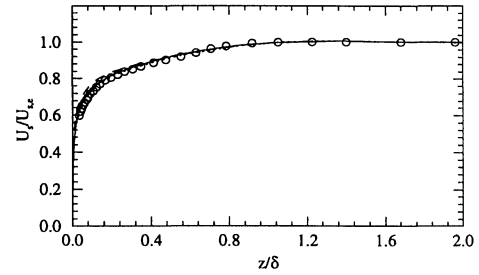
Figure 4 shows the streamwise evolution of some mean flow properties along the duct centerline. All models correctly predict the freestream velocity angle  $\gamma_e$  ( $= \tan^{-1}[V_e/U_e]$ , where the subscript  $e$  denotes boundary-layer edge value) along the centerline, which confirms that anisotropic effects are weak in this region with essentially minimal effects of viscosity. For consistency with the experimental results, the boundary-layer thickness  $\delta$  is defined as the location where the magnitude of the mean velocity was 99.5% of the freestream velocity. The model predictions are similar at the first three measuring stations ( $P_1$ – $P_3$ ); however, as expected the predictions diverge as the pressure-gradient effects become important at stations  $P_4$  and  $P_5$ . At these downstream stations, the anisotropic models yield a better prediction of  $\delta$ . The displacement thickness  $\delta^*$  predictions in Fig. 4c show that at the first measuring station all models underpredict the level of  $\delta^*$ , although all of the models display the correct qualitative trend throughout the duct. Overall, the composite model outperforms both the EASM and the EVM in predicting  $\delta^*$ . A similar result is evident in Fig. 4d for prediction



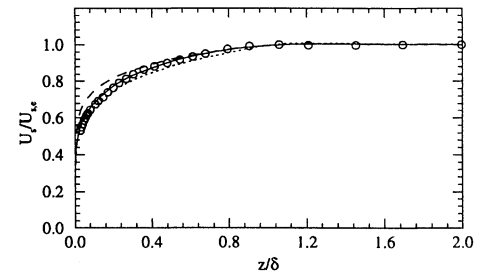
a)  $P_1$  ( $x = 1.39, y = 0.50$ )



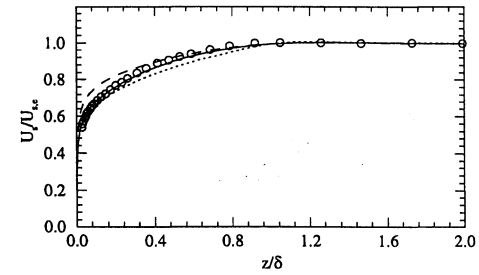
b)  $P_2$  ( $x = 2.23, y = 0.39$ )



c)  $P_3$  ( $x = 2.80, y = 0.11$ )



d)  $P_4$  ( $x = 3.60, y = -0.30$ )



e)  $P_5$  ( $x = 4.20, y = -0.10$ )

**Fig. 5 Streamwise velocity profiles at various S-duct locations:  $\circ$ , experiment; —, composite model; ---, EASM; and - - -, EVM.**

of the momentum thickness  $\theta$ . Furthermore, the composite model is better able to capture the local maximum at point  $P_2$  for both  $\delta^*$  and  $\theta$  and the boundary-layer growth downstream of station  $P_4$ .

Figure 5 shows the variation in the streamwise mean velocity  $U_x$  profiles at five different measuring stations. The location coordinates for the positions  $P_1$ – $P_5$  are given; the relative locations in the duct can be seen in Fig. 3. As shown, the predictions of the three models are quite good at the first three measuring stations. At stations  $P_4$  and  $P_5$ , the composite model outperforms the other two models in predicting the experimental distributions.

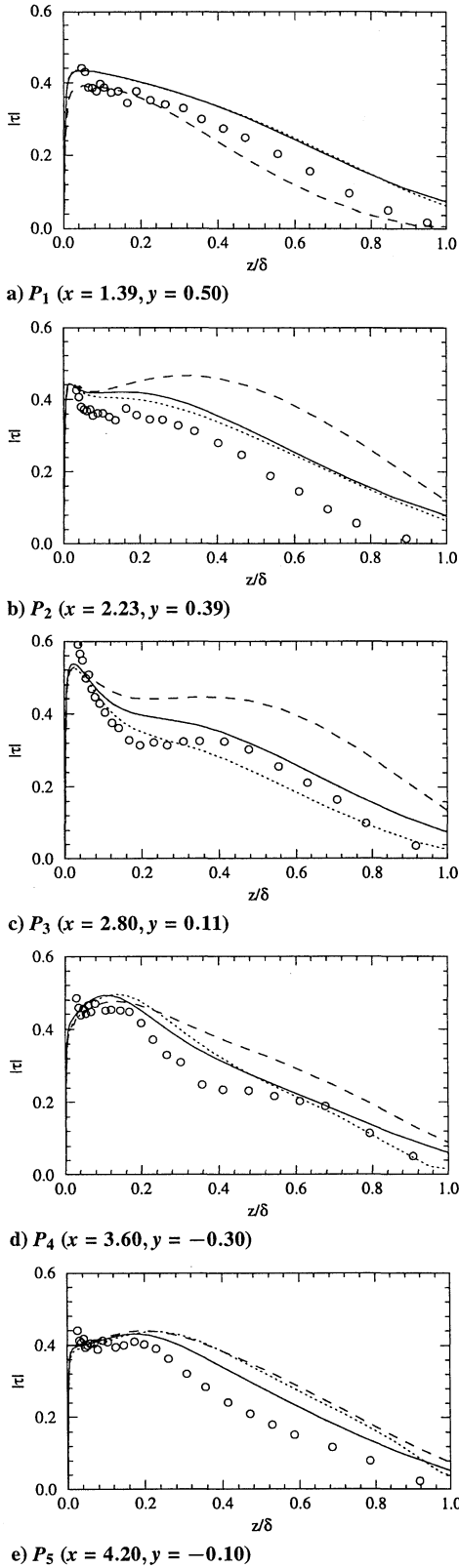


Fig. 6 Profiles of total shear stress in  $x$ - $y$  plane at various S-duct locations:  $\circ$ , experiment; —, composite model; ---, EASM; and -·-, EVM.

One justification for the use of higher-order turbulence closure models is the ability to extract a better representation of the turbulence in the flowfield. Because the algebraic closures used here can better account for both the stress and dissipation rate anisotropies, these models should provide better predictions of the turbulent flowfield. In Fig. 6, profiles of the total shear stress

$$|\tau| = \sqrt{\tau_{xz}^2 + \tau_{nz}^2} \quad (35)$$

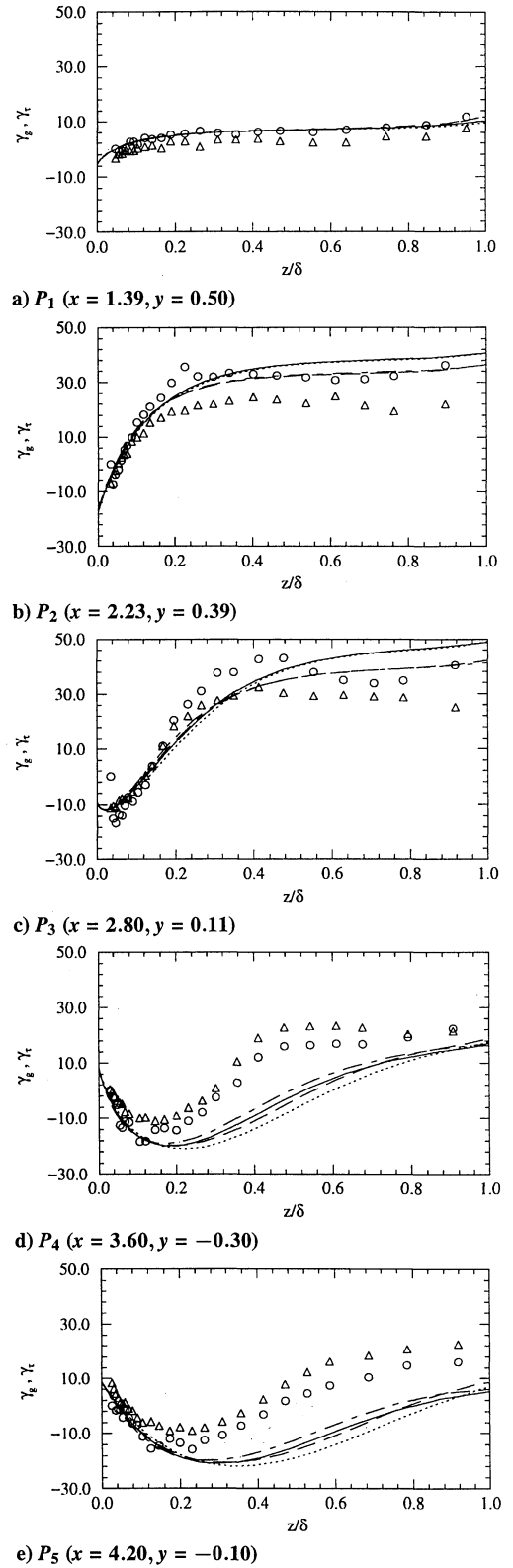
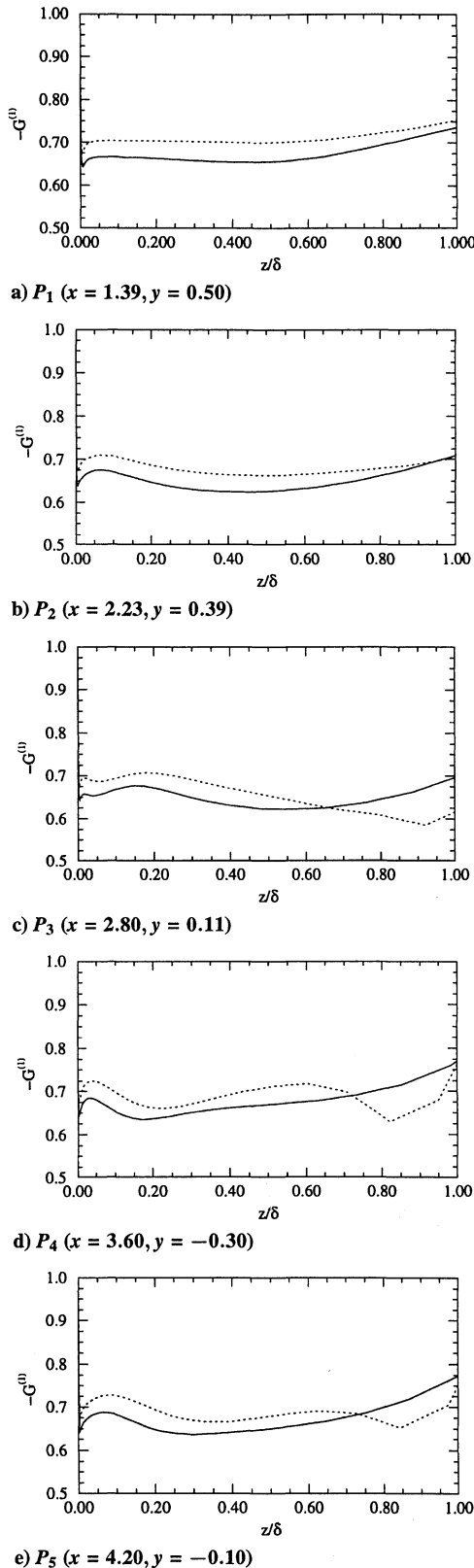


Fig. 7 Profiles of velocity-gradient vector direction  $\gamma_g$  and shear-stress vector direction  $\gamma_\tau$  at various S-duct locations:  $\circ$ ,  $\gamma_g$  experiment;  $\triangle$ ,  $\gamma_\tau$  experiment; —,  $\gamma_g$  composite model; ---,  $\gamma_\tau$  composite model; -·-,  $\gamma_g$  EASM; and -·-,  $\gamma_\tau$  EASM.

in the  $s$ - $n$  plane (see Fig. 3) are shown at each of the five measurement stations. At station  $P_1$ , all models deviate from the experimental points; the EVM provides the most accurate prediction. At  $P_2$  and  $P_3$ , the two explicit algebraic models more closely approximate the data; the EASM performs slightly better. However, farther downstream in the recovery region, the composite algebraic stress model begins to outperform the EASM, and then at  $P_5$  this model provides the best predictions. As the freestream is approached, all models converge to the same values.



**Fig. 8** Variation of  $G^{(1)}$  across S-duct at different streamwise locations: —, composite model and - - -, EASM.

Figure 7 shows profiles of the direction of the velocity-gradient vector and shear-stress vector along the duct, which are given by

$$\gamma_g = \tan^{-1} \left[ \frac{\partial U_n / \partial z}{\partial U_s / \partial z} \right] \quad (36)$$

$$\gamma_\tau = \tan^{-1} (\tau_{nz} / \tau_{sz}) \quad (37)$$

At the first three measurement stations, the two models perform equally and exhibit the same qualitative trends as the data. Farther downstream at stations  $P_4$  and  $P_5$ , the predictions diverge. Both the

composite model and the EASM show the characteristic lagging of the shear-stress vector behind the velocity-gradient vector, as in the experimental results<sup>11</sup>; however, the composite model provides a slightly better prediction of the magnitude levels. Recall that an obvious deficiency of the EVM model is that the shear-stress vector and the velocity-gradient vector are aligned everywhere.

As the results for the mean flow and turbulence quantities have shown, the composite model agrees more closely with the experimental results than the EASM and, of course, the EVM. These improvements are realized with a minimal increase in computational cost over that of the EVM. The inclusion of the anisotropic dissipation rate effects in the algebraic stress formulation modifies both the production of dissipation term through  $C_{\varepsilon 1}^*$  [Eq. (32)] and the turbulent Reynolds stresses through the scalar functions  $G^{(\lambda)}$  [Eq. (29)].

For the EASM,  $C_{\varepsilon 1}^* = C_{\varepsilon 1} = 1.44$ . In the new composite model,  $C_{\varepsilon 1}^* \approx 1.51$  and remains relatively constant throughout the boundary layer at the duct measuring stations  $P_1$ – $P_5$ . This value is also the same as the value that is obtained from the channel flow calibration shown in Fig. 2.

The scalar functions  $G^{(\lambda)}$  are simply related in the EASM by

$$G^{(1)} = -C_\mu^* \quad (38)$$

$$G^{(2)} = G^{(1)} \quad (39)$$

and

$$G^{(3)} = -2G^{(1)} \quad (40)$$

In the composite model, the  $G^{(\lambda)}$  have a more complex relationship:

$$G^{(1)} = -C_\mu^* - \mathcal{A}_1 C_\mu^* \left[ 1 - \frac{2}{3} \eta^2 (\beta_2 / \alpha_3) - 2\zeta^2 (\beta_1 / \alpha_2) \right] \quad (41)$$

$$G^{(2)} = G^{(1)} - (\beta_1 / \alpha_2) \mathcal{A}_1 = G^{(1)} - \mathcal{A}_2 \quad (42)$$

and

$$G^{(3)} = -2G^{(1)} - 2(\beta_2 / \alpha_3) \mathcal{A}_1 = -2G^{(1)} - 2\mathcal{A}_3 \quad (43)$$

The second term on the right in Eq. (41) has a nearly constant additive effect relative to the behavior of  $G^{(1)}$  in the EASM across most of the boundary layer (Fig. 8). Only in the outer part of the boundary layer at stations  $P_1$  and  $P_2$  do the predictions from the two models coincide. In the composite model, the effect of the linear term in the tensor expansion has been diminished; Fig. 8 shows a reduction in the value of  $G^{(1)}$  over half of the boundary layer in comparison with the EASM results. It can be verified that this reduction is partially offset by an increase in the values of  $G^{(2)}$  and  $G^{(3)}$  relative to the EASM values.

#### IV. Concluding Remarks

The performance of a composite EASM for the turbulent Reynolds stresses, which accounts for dissipation anisotropies, has been analyzed. This explicit algebraic model has been calibrated for application to wall-bounded turbulent flows by introducing a damping function factor into the destruction of dissipation term in the isotropic dissipation-rate equation. The coefficient in the production of dissipation term  $C_{\varepsilon 1}^*$  is now sensitized to both the mean strain rate and rotation rate fields, which results in a new, higher level for the production of dissipation. The Reynolds stresses are also directly affected by the dissipation rate anisotropy through the alteration of  $C_\mu^*$  in the nonlinear eddy viscosity.

In a validation comparison with an S-duct flow, the new model outperforms both the EVM and the EASM in predicting both mean and turbulent flow quantities. In the calculation, the value of  $C_{\varepsilon 1}^*$  increases relative to the EASM value for  $C_{\varepsilon 1}$  but remains relatively constant across the boundary layer. The scalar functions  $G^{(\lambda)}$  for the composite model are altered by the inclusion of the dissipation anisotropies. Whereas the value of the function  $G^{(1)}$  (linear term) in the composite model is less than the corresponding value in the EASM across most of the duct, the value of the nonlinear terms, represented through  $G^{(2)}$  and  $G^{(3)}$ , is greater than the corresponding value in the EASM across the duct.

The methodology and validation study presented show that the effects of dissipation rate anisotropy can be incorporated into an algebraic stress framework and applied to a complex flowfield at minimal additional computational cost. Although further validation studies involving external aerodynamic flows may be more challenging due



to the high Reynolds numbers and corresponding thin boundary layers, the present composite model can prove to be a robust predictive tool and, with its inclusion of anisotropic dissipation rate effects, an improved predictive tool for such flowfields.

### Acknowledgments

The first author received financial support from the Commission Suisse pour l'Encouragement de la Recherche Scientifique and Sulzer Brothers S.A. under Contract 3062.1. The third author also acknowledges the support of the European Research Community on Flow Turbulence and Combustion (ERCOFTAC) Leonhard Euler Research Center while in residence at École Polytechnique Fédérale de Lausanne as an ERCOFTAC Scientific Visitor. The authors thank M. Deville for his encouragement and helpful discussions throughout this study.

### References

- <sup>1</sup>Lumley, J. L., "Computational Modeling of Turbulent Flows," *Advances in Applied Mechanics*, Vol. 18, 1978, pp. 123-176.
- <sup>2</sup>Hallböck, M., Groth, J., and Johansson, A. V., "An Algebraic Model for Nonisotropic Turbulent Dissipation Rate in Reynolds Stress Closures," *Physics of Fluids, A*, Vol. 2, No. 10, 1990, pp. 1859-1866.
- <sup>3</sup>Speziale, C. G., and Gatski, T. B., "Analysis and Modeling of Anisotropies in the Dissipation Rate of Turbulence," *Journal of Fluid Mechanics*, Vol. 344, 1997, pp. 155-180.
- <sup>4</sup>Oberlack, M., "Non-Isotropic Dissipation in Non-Homogeneous Turbulence," *Journal of Fluid Mechanics*, Vol. 350, 1997, pp. 351-374.
- <sup>5</sup>Gatski, T. B., and Speziale, C. G., "On Explicit Algebraic Stress Models for Complex Turbulent Flows," *Journal of Fluid Mechanics*, Vol. 254, 1993, pp. 59-78.
- <sup>6</sup>Lauder, B. E., "An Introduction to Single-Point Closure Methodology," *Simulation and Modeling of Turbulent Flows*, edited by T. B. Gatski, M. Y. Hussaini, and J. L. Lumley, Oxford Univ. Press, New York, 1996, pp. 243-310.
- <sup>7</sup>Abid, R., Morrison, J. H., Gatski, T. B., and Speziale, C. G., "Prediction of Complex Aerodynamic Flows with Explicit Algebraic Stress Models," *AIAA Journal*, Vol. 34, No. 12, 1995, pp. 2632-2635.

<sup>8</sup>Gatski, T. B., "Prediction of Airfoil Characteristics Using Higher-Order Turbulent Models," NASA TM-11024, April 1996.

<sup>9</sup>Abid, R., Rumsey, C., and Gatski, T. B., "Prediction of Nonequilibrium Turbulent Flows with Explicit Algebraic Stress Models," *AIAA Journal*, Vol. 33, No. 11, 1995, pp. 2026-2031.

<sup>10</sup>Xu, X.-H., and Speziale, C. G., "Explicit Algebraic Stress Model of Turbulence with Anisotropic Dissipation," *AIAA Journal*, Vol. 34, No. 10, 1996, pp. 2186-2189.

<sup>11</sup>Bruns, J., and Truong, T.-V., "Flow in an S-Shaped Duct," *Proceedings of the 2nd International Conference on Experimental Fluid Mechanics*, edited by M. Onorato, Levrotto and Bella, Turin, Italy, 1994, pp. 679-687.

<sup>12</sup>Speziale, C. G., and Xu, X.-H., "Towards the Development of Second-Order Closure Models for Non-Equilibrium Turbulent Flows," *International Journal of Heat and Fluid Flow*, Vol. 17, No. 3, 1996, pp. 238-244.

<sup>13</sup>Speziale, C. G., Sarkar, S., and Gatski, T. B., "Modelling the Pressure-Strain Correlation of Turbulence: An Invariant Dynamical Systems Approach," *Journal of Fluid Mechanics*, Vol. 227, 1991, pp. 245-272.

<sup>14</sup>Rogers, M. M., Moin, P., and Reynolds, W. C., "The Structure and Modeling of the Hydrodynamic and Passive Scalar Fields in Homogeneous Turbulent Shear Flow," Stanford Univ., TR TF-25, Stanford, CA, Aug. 1986.

<sup>15</sup>Lafer, J., "Investigation of Turbulent Flow in a Two-Dimensional Channel," NACA TR 1053, 1951.

<sup>16</sup>Truong, T.-V., and Brunet, M., "Test Case T1: Boundary Layer in a S-Shaped Channel," *Numerical Simulation of Unsteady Flows and Transition to Turbulence*, edited by O. Pironneau, W. Rodi, I. L. Rymming, A. M. Savill, and T.-V. Truong, Cambridge Univ. Press, Cambridge, England, UK, 1992, pp. 78-115.

<sup>17</sup>Chen, H. C., and Patel, V. C., "Near-Wall Turbulence Models for Complex Flows Including Separation," *AIAA Journal*, Vol. 26, No. 6, 1988, pp. 641-648.

<sup>18</sup>Jongen, T., and Marx, Y., "An Efficient and Robust Numerical Method for Simulating Turbulent Fluid Flows," *Proceedings of the Second ECCO-MAS Conference on Numerical Methods in Engineering*, edited by J.-A. Désidéri, C. Hirsch, P. Le Tallec, E. Oñate, M. Pandolfi, J. Périaux, and E. Stein, Wiley-Interscience, New York, 1996, pp. 366-373.

C. G. Speziale  
Associate Editor

## NEW AIAA PROFESSIONAL DEVELOPMENT SHORT COURSE

# DESIGN OF COMPOSITE STRUCTURES

**April 17-19, 1998**  
**Long Beach, California**

This introductory course covers the structural design process and experience with composite materials, manufacturing processes, materials and configuration selection, joints and attachments, design failure criteria, optimization concepts, design analysis philosophy and future trends in design.

Specifically, this course explores the nature of various aspects to be considered when designing composite structures. Examples used during the course will emphasize aircraft structures; however, the instructor will explore related applications in spacecraft, automobile, and other fields.

**Key Topics**

- Review the structural design process
- Learn new and different design characteristics for composite structures
- Become acquainted with manufacturing processes for composites
- Be able to rationally compare one material to others
- Evaluate alternative structural configurations

**Instructor**

Dr. Robert M. Jones is currently Professor of Engineering Science and Mechanics at Virginia Polytechnic Institute and State University. He is an Associate Fellow of AIAA.

**Course Fee**

AIAA Member: \$895 • Nonmember: \$995

**Special Offer!** Attend this short course, paying the standard member or nonmember fee, and receive a **FREE** registration (sessions and exhibits only) to the **39th AIAA/ASME/ASCE/AHS/ASC Structures, Structural Dynamics, and Materials Conference and Exhibit** in Long Beach, California!


**Course Outline**

Introduction  
The Structural Design Process  
Structural Design Experience with Composite Materials  
Manufacturing Processes  
Materials Selection  
Configuration Selection  
Joints and Attachments  
Design Failure Criteria  
Optimization Concepts  
Design Analysis Philosophy for Composite Structures  
Future Trends in Design

**For More Information**

**Call AIAA Customer Service:**

**800/639-AIAA (U.S. only),**  
**703/264-7500,**  
**fax 703/264-7551**  
**or visit our Web site at**  
**<http://www.aiaa.org>**  
**for a complete course outline and to register.**



American Institute of  
Aeronautics and Astronautics